Available online at www.sciencedirect.com
ScienceDirect
Comput. Methods Appl. Mech. Engrg. 370 (2020) 113213
Computer methods in applied mechanics and engineering
www.elsevier.com/locate/cma

A multinumerics scheme for incompressible two-phase flow

Bryan Doyle[a,1], Beatrice Riviere[a,*,1], Michael Sekachev[b]

[a] *Rice University, 6100 Main St, Houston, TX 77005, United States of America*
[b] *Total, 1201 Louisiana St, Houston, TX 77002, United States of America*

Available online xxxx

Abstract

The incompressible two-phase flow problem is solved by a method that combines cell-centered finite volume with discontinuous Galerkin in non-overlapping subdomains. The primary unknowns are the wetting phase pressure and the capillary pressure. The nonlinear equations are solved fully implicitly at each time step. Fluxes at the interface between subdomains are defined implicitly to allow for seamless propagation of saturation fronts. Numerical results show the robustness and efficiency of the method for homogeneous and heterogeneous porous media.

MSC: 65M08; 65M60

Keywords: Fully implicit; Two-phase; Discontinuous Galerkin; Finite volume; Heterogeneities

1. Introduction

This work formulates a numerical method for solving the incompressible two-phase flow problem in porous media. Simulation of multiphase flow at the Darcy scale is an essential part of reservoir management for the oil and gas industry. Petroleum engineers are concerned with the accurate prediction of the propagation of the injected and resident phases into the reservoir. Reservoirs are characterized by strong rock heterogeneities, which may pose a challenge for numerical modeling. Conservation of mass for each phase yields a mathematical model that is a coupled system of nonlinear partial differential equations. Since the mathematical model is based on mass balance for each phase, the numerical methods are required to be locally mass conservative in a discrete sense. Finite difference methods, finite volume methods, mixed finite element methods and discontinuous Galerkin methods are known to be locally mass conservative methods for elliptic problems. These methods have been applied to the multiphase flow problem in porous media (see for instance [1–3]) and they each have pros and cons. Finite difference and finite volume methods are mostly used with piecewise constants whereas mixed finite element methods and discontinuous Galerkin methods are easily employed with high order polynomial approximations. Ideal numerical methods for modeling two-phase flow in porous media should have negligible numerical diffusion, they should be robust and accurate on structured and unstructured grids (even with highly distorted grid cells); they should handle heterogeneities and anisotropy; and finally their computational cost should be reasonable.

* Corresponding author.
E-mail address: riviere@rice.edu (B. Riviere).
[1] Funding by NSF-DMS 1913291 is acknowledged.

https://doi.org/10.1016/j.cma.2020.113213

We propose a multinumeric method that partitions the domain into subdomains and employs in each subdomain either finite volume or discontinuous Galerkin. The resulting method benefits from the positive features of the two types of discretization at a total reduced computational cost. In parts of the domain where more accuracy is required, the discontinuous Galerkin discretization is employed whereas in other parts of the domain finite volume methods are used. The idea of combining discontinuous Galerkin and cell-centered finite volume has been proposed in the literature for simple model problems. In [4,5], we formulated the multinumeric method on Voronoi meshes for convection–diffusion problems. A theoretical convergence was proved in [6] for transport equations. However, we point out that in this proposed work, the numerical fluxes at the interface between the discontinuous Galerkin and finite volume subdomains differ from those used in [4–6].

Reservoir simulators used by practitioners in the oil and gas industry are mainly based on two-point flux cell-centered finite volume (FV) methods because of the simplicity of these methods and their low computational cost [7–9]. However, such finite volume methods are numerically diffusive, they suffer from grid distortion and they cannot handle full anisotropy. It is worth noting that several finite-volume schemes, different from the simple two-point flux methods, have been proposed in the literature to address the issues of grid distortion and anisotropy (see [10,11] and references herein). The class of interior penalty discontinuous Galerkin (DG) methods has been applied to multiphase flow in porous media [12–17]. They have very little numerical diffusion, they do not suffer from grid distortion and they can handle full anisotropy. Their main drawback is their high computational cost. An important motivation for having different discretizations in different domains is that this approach takes advantage of both the accuracy of DG in regions of interest, such as regions containing local features (channels, barriers, pinch-outs, wells), and the efficiency and low cost of two-point flux FV in the rest of the domain. By increasing the order of approximation in the DG regions, we can obtain higher accuracy locally without having to change the grid. In addition, since DG methods are variational methods, they do not suffer from grid distortion. This allows the use of unstructured grids that coincide with local features (pinch-outs for instance) in the DG regions whereas a much simpler Cartesian grid can be used in the FV regions.

Another important consideration, besides the choice of the spatial discretization and order of polynomial approximation, is the choice of time-stepping and linearization of the discrete equations [18–20]. The IMPES method solves for one pressure implicitly and one saturation explicitly in time; the semi-implicit method solves each equation implicitly and sequentially; the fully implicit method solves for both unknowns at once. The most popular choice of primary unknowns is one phase pressure and one phase saturation. Other choices used in the literature include two pressures [21]. Recently, Bastian proposed to solve for the wetting phase pressure and the capillary pressure with a fully implicit discontinuous Galerkin scheme [16] and showed that the method performs well for highly heterogeneous media. Following [16], we will solve the discrete equations fully implicitly for the wetting phase pressure and capillary pressure.

An outline of the paper is as follows. Section 2 defines the mathematical model for two-phase flow with the physical wetting phase pressure and capillary pressure as primary unknowns. The multinumeric scheme is introduced in Section 3. Numerical results in Section 4 show the robustness and accuracy of the algorithm. Conclusions follow in Section 5.

2. Model problem

The incompressible two-phase flow problem in a porous medium is modeled by a system of mass balance equations for each phase, coupled with closure relations.

$$\frac{\partial(\phi\rho_\alpha s_\alpha)}{\partial t} - \nabla\cdot(\rho_\alpha\lambda_\alpha K\nabla p_\alpha) = 0, \quad \alpha = \mathrm{w},\ \mathrm{n}, \tag{1}$$

$$s_\mathrm{w} + s_\mathrm{n} = 1, \tag{2}$$

$$p_c = p_\mathrm{n} - p_\mathrm{w}. \tag{3}$$

The saturation and pressure of the wetting phase (resp. non-wetting phase) are denoted by s_w, p_w (resp. s_n, p_n). The difference between phase pressures is the capillary pressure, p_c, which is a given function of the wetting phase saturation [18]. The Brooks–Corey and Van Genuchten models are popular choices for the capillary pressure [22,23]. Our proposed method can handle either one, and for convenience, we have chosen the Brooks–Corey model:

$$p_c = \frac{p_e}{s_\mathrm{w}^\theta}, \tag{4}$$

where the entry pressure p_e and the exponent θ are given constants. We can solve for the wetting phase saturation as a function ψ of capillary pressure. To have well-defined values, the function ψ is regularized (as in [16]):

$$s_{\mathrm{w}} = \psi(p_c) = \begin{cases} 1 - \theta \frac{p_c - p_e}{p_e} & \text{if } p_c < p_e, \\ \left(\frac{p_e}{p_c}\right)^{\theta} & \text{if } p_c \geq p_e. \end{cases} \tag{5}$$

The absolute permeability of the medium is denoted by K and the phase mobility, λ_α, is defined by:

$$\lambda_\alpha = \frac{k_{r_\alpha}}{\mu_\alpha}, \quad \alpha = \mathrm{w}, \mathrm{n}. \tag{6}$$

The total mobility λ_t is the sum of the phase mobilities ($\lambda_t = \lambda_{\mathrm{w}} + \lambda_{\mathrm{n}}$). The porosity ϕ and absolute permeability K are positive functions that vary in space. The phase density ρ_α and phase viscosity μ_α are positive constants. The phase relative permeability k_{r_α} is a function of the wetting phase saturation. We select for primary unknowns the wetting phase pressure and the capillary pressure. After manipulation (see [16]), the system (1)–(3) is rewritten as:

$$-\nabla \cdot (\lambda_t K \nabla p_{\mathrm{w}} + \lambda_{\mathrm{n}} K \nabla p_c) = 0, \tag{7}$$

$$-\frac{\partial(\phi\psi)}{\partial t} - \nabla \cdot (\lambda_{\mathrm{n}} K \nabla p_c) + \nabla \cdot \left(\frac{\lambda_{\mathrm{n}}}{\lambda_t}\boldsymbol{u}\right) = 0. \tag{8}$$

Note that it is guaranteed that λ_t is strictly positive. The velocity $\boldsymbol{u} = -\lambda_t K \nabla p_{\mathrm{w}}$ is the wetting phase velocity up to a multiplicative scalar. The functions $\lambda_{\mathrm{w}}, \lambda_{\mathrm{n}}, \lambda_t$ and ψ are nonlinear functions of p_c. The system (7)–(8) is completed by initial and boundary conditions. The boundary of the domain is partitioned into Dirichlet and Neumann boundaries, Γ_{D} and Γ_{N} respectively.

$$p_{\mathrm{w}} = g_{\mathrm{w}}, \quad p_c = g_{\mathrm{n}} - g_{\mathrm{w}}, \quad \text{on} \quad \Gamma_{\mathrm{D}}, \tag{9}$$

$$-\lambda_{\mathrm{w}} K \nabla p_{\mathrm{w}} \cdot \boldsymbol{n} = j_w, \quad -\lambda_{\mathrm{n}} K \nabla (p_c + p_{\mathrm{w}}) \cdot \boldsymbol{n} = j_n, \quad \text{on} \quad \Gamma_{\mathrm{N}}. \tag{10}$$

Finally, a wetting phase saturation is prescribed in the domain at the initial time, which yields an initial capillary pressure denoted by p_c^0. For simplicity, gravity is neglected and only a single capillary pressure law is used in the whole domain. The scheme proposed in the following section can be extended to account for gravity and varying capillary pressure laws.

3. Multinumeric DG-FV scheme

In this section, we introduce a fully discrete scheme for (7)–(10) that combines the interior penalty discontinuous Galerkin and the cell-centered finite volume methods.

3.1. Notation and discrete spaces

The domain Ω is subdivided into M non-overlapping subdomains Ω_i. On each subdomain, the discrete solution will either be a DG solution or a FV solution. We denote by Ω^{FV} (resp. Ω^{DG}) the union of the subdomains where the finite volume (resp. discontinuous Galerkin) method is used. Let $\mathcal{T}_h^{\mathrm{FV}}$ be a shape-regular mesh of Ω^{FV}, and let $\mathcal{T}_h^{\mathrm{DG}}$ be a shape-regular mesh of Ω^{DG}. We assume that $\mathcal{T}_h^{\mathrm{FV}}$ is made of rectangular elements in 2D and boxes in 3D. There is no restriction on the shape of elements in Ω^{DG}. Let h denote the maximum diameter of the elements in $\mathcal{T}_h^{\mathrm{FV}} \cup \mathcal{T}_h^{\mathrm{DG}}$. The interface between the subregions is denoted by Γ^{DF}; we assume the meshes $\mathcal{T}_h^{\mathrm{FV}}$ and $\mathcal{T}_h^{\mathrm{DG}}$ align on Γ^{DF}. We denote by $\Gamma_{h,0}^{\mathrm{FV}}$ the set of all interior faces of $\mathcal{T}_h^{\mathrm{FV}}$ and by $\Gamma_{h,0}^{\mathrm{DG}}$ the set of all interior faces of $\mathcal{T}_h^{\mathrm{DG}}$. We denote by $\Gamma_{\mathrm{D}}^{\mathrm{FV}}$ and $\Gamma_{\mathrm{N}}^{\mathrm{FV}}$ the set of all Dirichlet and Neumann boundary faces on $\partial\Omega^{\mathrm{FV}} \cap \partial\Omega$. Similarly, we denote by $\Gamma_{\mathrm{D}}^{\mathrm{DG}}$ and $\Gamma_{\mathrm{N}}^{\mathrm{DG}}$ the set of all Dirichlet and Neumann boundary faces on $\partial\Omega^{\mathrm{DG}} \cap \partial\Omega$. Finally we will use the notation:

$$\Gamma_h^{\mathrm{FV}} = \Gamma_{h,0}^{\mathrm{FV}} \cup \Gamma_{\mathrm{D}}^{\mathrm{FV}} \cup \Gamma_{\mathrm{N}}^{\mathrm{FV}}, \tag{11}$$

$$\Gamma_h^{\mathrm{DG}} = \Gamma_{h,0}^{\mathrm{DG}} \cup \Gamma_{\mathrm{D}}^{\mathrm{DG}} \cup \Gamma_{\mathrm{N}}^{\mathrm{DG}}. \tag{12}$$

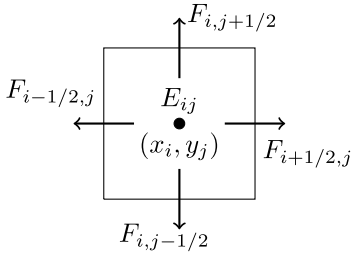

Fig. 1. Flux definitions and directions for element $E_{ij} \in \Omega^{\mathrm{FV}}$.

The discrete approximations of wetting phase pressure and capillary pressure belong to the space of discontinuous linears in the DG region and discontinuous constants in the FV region. Let $\mathbb{P}_r(E)$ be the space of polynomials of degree r on one mesh element E. The discrete space X_h is defined by:

$$X_h = \left\{ v \in L^2(\Omega) : v|_E \in \mathbb{P}_1(E), \quad \forall E \in \mathcal{T}_h^{\mathrm{DG}}; \quad v|_E \in \mathbb{P}_0(E), \quad \forall E \in \mathcal{T}_h^{\mathrm{FV}} \right\}. \tag{13}$$

It is also possible to choose piecewise polynomials of degree $r \geq 2$ in the DG regions. For convenience, we employ piecewise linears in this work. As usual for discontinuous polynomial approximations, we introduce jump and average of functions across faces. For each interior face e, we fix a unit normal vector $\boldsymbol{n}_e$. If the face e belongs to the interface Γ^{DF}, the normal vector is chosen so that it points from the DG region to the FV region. This choice is only a matter of convenience. The normal vector coincides with the outward normal vector to $\partial\Omega$ if e belongs to the boundary. Let us denote by E_e^- and E_e^+ the mesh elements that share the face e with the unit vector $\boldsymbol{n}_e$ pointing from E_e^- to E_e^+. We can now uniquely define the jump $[\cdot]$ and average $\{\cdot\}$ operators.

$$[v]|_e = v|_{E_e^-} - v|_{E_e^+}, \quad \{v\}|_e = \delta_e^- v|_{E_e^-} + \delta_e^+ v|_{E_e^+}, \quad v \in X_h.$$

The scalars δ_e^-, δ_e^+ are positive weights that sum to one. It has been observed in the literature that the amount of overshoot and undershoot in the DG solutions is greatly reduced if the weights depend on the permeability field. Therefore, following [24] we define:

$$\delta_e^- = \frac{K|_{E_e^+}}{K|_{E_e^-} + K|_{E_e^+}}, \quad \delta_e^+ = \frac{K|_{E_e^-}}{K|_{E_e^-} + K|_{E_e^+}}. \tag{14}$$

We observe that we recover the usual arithmetic average with weights equal to $1/2$ if the permeability is constant in the domain. By convention, the notations $[\cdot]$ and $\{\cdot\}$ are used on boundary faces and in this case, jump and average operators coincide with the trace operator. Finally we will use the harmonic average function $\mathcal{H}$:

$$\mathcal{H}(a, b) = \frac{2ab}{a+b}, \quad \forall a > 0, b > 0.$$

3.2. Nonlinear forms in finite volume subdomains

We will describe the cell-centered finite volume method for two-dimensional domains for simplicity [25]. The method is defined similarly in three dimensions. Let $E_{ij} \in \mathcal{T}_h^{\mathrm{FV}}$ be a rectangle $(x_{i-1/2}, x_{i+1/2}) \times (y_{j-1/2}, y_{j+1/2})$ with center of gravity (x_i, y_j) and let us denote by v_{ij} the restriction on E_{ij} of a test function $v \in X_h$. Furthermore, we define the mesh spacing in the x and y directions for E_{ij} as

$$h_i^x = x_{i+1/2} - x_{i-1/2}, \quad h_j^y = y_{j+1/2} - y_{j-1/2}. \tag{15}$$

The diffusive fluxes from (7) are discretized by finite difference. Fig. 1 shows the element E_{ij} with its discrete fluxes $F_{i-1/2,j}$, $F_{i+1/2,j}$, $F_{i,j-1/2}$, and $F_{i,j+1/2}$ along the right, left, top, and bottom edges of element E_{ij}, respectively. We will explicitly define the flux along the right vertical edge, denoted by $e_{i+1/2,j}$. The fluxes on the other three edges are defined in a similar manner.

For the diffusive term $-\nabla \cdot (K\lambda_t \nabla p_{\mathrm{w}})$, the finite volume flux on $e_{i+1/2,j}$ is defined following [25]:

$$F_{i+1/2,j}^{\mathrm{w}} = \begin{cases} -h_j^y \mathcal{H}\left(\frac{(K\lambda_t)_{ij}}{h_i^x}, \frac{(K\lambda_t)_{i+1,j}}{h_{i+1}^x}\right)\left((P_w)_{i+1,j} - (P_w)_{ij}\right) & \text{if } e_{i+1/2,j} \in \Gamma_{0,h}^{\mathrm{FV}}, \\ -2\frac{h_j^y}{h_i^x}(K\lambda_t)_{ij}\left(g_{\mathrm{w}}(x_{i+1/2}, y_j) - (P_w)_{ij}\right) & \text{if } e_{i+1/2,j} \in \Gamma_{\mathrm{D}}^{\mathrm{FV}}. \end{cases}$$

Analogously, we define the flux $F^c_{i+1/2,j}$ corresponding to the finite volume discretization of the term $-\nabla\cdot(K\lambda_{\mathrm{n}}\nabla p_c)$ on the edge $e_{i+1/2,j}$.

$$F^c_{i+1/2,j}=\begin{cases}-h^y_j\mathcal{H}\left(\frac{(K\lambda_{\mathrm{n}})_{ij}}{h^x_i},\frac{(K\lambda_{\mathrm{n}})_{i+1,j}}{h^x_{i+1}}\right)\left((P_c)_{i+1,j}-(P_c)_{ij}\right) & \text{if } e_{i+1/2,j}\in\Gamma^{\mathrm{FV}}_{0,h},\\ -2\frac{h^y_j}{h^x_i}(K\lambda_{\mathrm{n}})_{ij}\left(g_c(x_{i+1/2},y_j)-(P_c)_{ij}\right) & \text{if } e_{i+1/2,j}\in\Gamma^{\mathrm{FV}}_{\mathrm{D}}.\end{cases}$$

Define the total flux as the sum of the two diffusive fluxes:

$$F_{i+1/2,j}=F^w_{i+1/2,j}+F^c_{i+1/2,j},\tag{16}$$

and extend it to zero for faces on the Neumann boundary. We can now write the finite volume discretization of (7):

$$a_{\mathrm{F}}(P_c,P_w,v)=\sum_{E_{ij}\in\mathcal{T}^{\mathrm{FV}}_h}\left(-F_{i-1/2,j}+F_{i+1/2,j}-F_{i,j-1/2}+F_{i,j+1/2}\right)v_{ij},\tag{17}$$

for all P_c, P_w, v in X_h.

We discretize the fluxes for the hyperbolic term in (8) similarly. As above, let us write the finite volume flux for the vertical edge $e_{i+1/2,j}$. If that edge is an interior edge, the upwinding term is defined below:

$$\left(\frac{\lambda_{\mathrm{n}}}{\lambda_t}\right)^{\uparrow}_{i+1/2,j}=\begin{cases}\frac{\lambda_{\mathrm{n}}(\psi((P_c)_{ij}))}{\lambda_t(\psi((P_c)_{ij}))} & \text{if } (P_w)_{i+1,j}<(P_w)_{ij},\\ \frac{\lambda_{\mathrm{n}}(\psi((P_c)_{i+1,j}))}{\lambda_t(\psi((P_c)_{i+1,j}))} & \text{if } (P_w)_{i+1,j}\geq(P_w)_{ij}.\end{cases}\tag{18}$$

For an edge $e_{i+1/2,j}$ that belongs to $\Gamma^{\mathrm{FV}}_{\mathrm{D}}$, the upwinding is defined as in (18) with the values $(P_{\mathrm{w}})_{i+1,j}$ and $(P_c)_{i+1,j}$ replaced by $g_{\mathrm{w}}(x_{i+1/2,j},y_j)$ and $\left(g_{\mathrm{n}}(x_{i+1/2,j},y_j)-g_{\mathrm{w}}(x_{i+1/2,j},y_j)\right)$ respectively. The finite volume flux corresponding to $\nabla\cdot((\lambda_{\mathrm{n}}/\lambda_t)\boldsymbol{u})$ in (8) is therefore defined on $e_{i+1/2,j}$ by:

$$G^w_{i+1/2,j}=\begin{cases}-h^y_j\left(\frac{\lambda_{\mathrm{n}}}{\lambda_t}\right)^{\uparrow}_{i+1/2,j}\mathcal{H}\left(\frac{(K\lambda_t)_{ij}}{h^x_i},\frac{(K\lambda_t)_{i+1,j}}{h^x_{i+1}}\right)\left((P_w)_{i+1,j}-(P_w)_{ij}\right) & \text{if } e_{i+1/2,j}\in\Gamma^{\mathrm{FV}}_{h,0},\\ -2\frac{h^y_j}{h^x_i}\left(\frac{\lambda_{\mathrm{n}}}{\lambda_t}\right)^{\uparrow}_{i+1/2,j}(K\lambda_t)_{ij}\left(g_{\mathrm{w}}(x_{i+1/2},y_j)-(P_w)_{ij}\right) & \text{if } e_{i+1/2,j}\in\Gamma^{\mathrm{FV}}_{\mathrm{D}}.\end{cases}$$

Define

$$G_{i+1/2,j}=G^w_{i+1/2,j}+F^c_{i+1/2,j},\tag{19}$$

and extend it to zero for Neumann faces. Similarly, we define the fluxes $G_{i-1/2,j}$, $G_{i,j+1/2}$ and $G_{i,j-1/2}$ for the other edges of the element E_{ij}. We then write the finite volume discretization for the diffusion and convection terms:

$$b_{\mathrm{F}}(P_c,P_w,v)=\sum_{E_{ij}\in\mathcal{T}^{\mathrm{FV}}_h}\left(-G_{i-1/2,j}+G_{i+1/2,j}-G_{i,j-1/2}+G_{i,j+1/2}\right)v_{ij},\tag{20}$$

for all P_c, P_w, v in X_h.

3.3. Nonlinear forms in discontinuous Galerkin subdomains

We employ the incomplete interior penalty discontinuous Galerkin method for discretizing the elliptic operators in (7), (8) in the DG subdomains and we employ an upwind technique for the nonlinear hyperbolic operator in (8). We skip the derivation of the forms for simplicity [26]. The DG form for (7) is

$$a_{\mathrm{D}}(P_c,P_w,v)=\sum_{E\in\mathcal{T}^{\mathrm{DG}}_h}\int_E\left(\lambda_t(\psi(P_c))K\nabla P_w+\lambda_{\mathrm{n}}(\psi(P_c))K\nabla P_c\right)\cdot\nabla v+\sum_{e\in\Gamma^{\mathrm{DG}}_{h,0}\cup\Gamma^{\mathrm{DG}}_{\mathrm{D}}}\int_e\frac{\sigma_0}{h}[P_w][v]$$
$$-\sum_{e\in\Gamma^{\mathrm{DG}}_{h,0}\cup\Gamma^{\mathrm{DG}}_{\mathrm{D}}}\int_e\{\lambda_t(\psi(P_c))K\nabla P_w\cdot\boldsymbol{n}_e\}[v]-\sum_{e\in\Gamma^{\mathrm{DG}}_{h,0}\cup\Gamma^{\mathrm{DG}}_{\mathrm{D}}}\int_e\{\lambda_{\mathrm{n}}(\psi(P_c))K\nabla P_c\cdot\boldsymbol{n}_e\}[v],\tag{21}$$

for any P_c, P_w, v in X_h. The penalty parameter σ_0 is defined by [16]

$$\sigma_0|_e = 2\mathcal{H}\left(\lambda_t(\psi(P_c|_{E_e^+}))K|_{E_e^+}, \lambda_t(\psi(P_c|_{E_e^-}))K|_{E_e^-}\right), \quad e = \partial E_e^+ \cap \partial E_e^-. \tag{22}$$

The DG form for (8) is

$$\begin{aligned} b_{\mathrm{D}}(P_c, P_w, v) = &\sum_{E\in\mathcal{T}_h^{\mathrm{DG}}}\int_E \lambda_{\mathrm{n}}(\psi(P_c))K\nabla P_c\cdot\nabla v + \sum_{e\in\Gamma_{h,0}^{\mathrm{DG}}\cup\Gamma_{\mathrm{D}}^{\mathrm{DG}}}\int_e \frac{\sigma_1}{h}[P_c][v] \\ &- \sum_{e\in\Gamma_{h,0}^{\mathrm{DG}}\cup\Gamma_{\mathrm{D}}^{\mathrm{DG}}}\int_e \{\lambda_{\mathrm{n}}(\psi(P_c))K\nabla P_c\cdot\boldsymbol{n}_e\}[v] + \sum_{E\in\mathcal{T}_h^{\mathrm{DG}}}\int_E \lambda_{\mathrm{n}}(\psi(P_c))K\nabla P_w\cdot\nabla v \\ &+ \sum_{e\in\Gamma_{h,0}^{\mathrm{DG}}\cup\Gamma_{\mathrm{D}}^{\mathrm{DG}}}\int_e \left(\frac{\lambda_{\mathrm{n}}(\psi(P_c))}{\lambda_t(\psi(P_c))}\right)^{\uparrow} U_e[v], \end{aligned} \tag{23}$$

for any P_c, P_w, v in X_h. The discrete flux is defined by

$$U_e = -\{\lambda_t(\psi(P_c))K\nabla P_w\cdot\boldsymbol{n}_e\} + \frac{\sigma_0}{h}[P_w], \quad e\in\Gamma_{h,0}^{\mathrm{DG}}, \tag{24}$$

$$U_e = -\lambda_t(\psi(P_c))K\nabla P_w\cdot\boldsymbol{n}_e + \frac{\sigma_0}{h}(P_w - g_{\mathrm{w}}), \quad e\in\Gamma_{\mathrm{D}}^{\mathrm{DG}}. \tag{25}$$

The upwind value on a face $e\in\Gamma_{0,h}^{\mathrm{DG}}$ is defined as follows:

$$\left(\frac{\lambda_{\mathrm{n}}}{\lambda_t}\right)^{\uparrow} = \begin{cases} \frac{\lambda_{\mathrm{n}}(\psi(P_c))}{\lambda_t(\psi(P_c))}\big|_{E_e^-}, & \text{if} \quad U_e > 0, \\ \frac{\lambda_{\mathrm{n}}(\psi(P_c))}{\lambda_t(\psi(P_c))}\big|_{E_e^+}, & \text{if} \quad U_e \le 0. \end{cases} \tag{26}$$

The upwind value on a boundary face $e\in\Gamma_{\mathrm{D}}^{\mathrm{DG}}$ is defined as in (26) with the function $P_c|_{E_e^+}$ replaced by $(g_{\mathrm{n}} - g_{\mathrm{w}})$. Finally, the penalty parameter σ_1 in (23) is given by:

$$\sigma_1 = 4\{\lambda_{\mathrm{n}}(\psi(P_c))\}\,\mathcal{H}(K|_{E_e^-}, K|_{E_e^+}). \tag{27}$$

3.4. Discretization of fluxes at the interface between FV and DG subdomains

The main contribution of this work is to couple two different discretization methods through appropriate handling of the fluxes across the interface Γ^{DF}. Multiplying (7) by a test function $v\in X_h$, integrating by parts, and extracting the terms involving the interface Γ^{DF} we obtain:

$$-\sum_{e\in\Gamma^{\mathrm{DF}}}\int_e \lambda_t K\nabla p_{\mathrm{w}}\cdot\boldsymbol{n}_e[v] - \sum_{e\in\Gamma^{\mathrm{DF}}}\int_e \lambda_{\mathrm{n}}K\nabla p_c\cdot\boldsymbol{n}_e[v]. \tag{28}$$

We point out that the choice of the normal vector on e on Γ^{DF} means that the jump $[v]$ in (28) is equal to the difference $(v|_{\Omega^{\mathrm{DG}}} - v|_{\Omega^{\mathrm{FV}}})$. Let us fix $e\in\Gamma^{\mathrm{DF}}$ and for readability, let us denote by E^{DG} and E^{FV} the mesh elements that belong to the DG and FV regions respectively such that $e = \partial E^{\mathrm{DG}}\cap\partial E^{\mathrm{FV}}$. It is clear that the direct computation of the gradient ∇p_{w} is feasible in the DG region but that it reduces to zero in the interior of elements in the FV region. We naturally propose to approximate the gradient by a first order finite difference, which is straightforward because the mesh elements in the finite volume region are rectangles or boxes.

$$K\lambda_t\nabla p_{\mathrm{w}}\cdot\boldsymbol{n}_e \approx \delta_{\mathrm{DG}}K|_{E^{\mathrm{DG}}}\lambda_t(\psi(p_c|_{E^{\mathrm{DG}}}))\nabla p_{\mathrm{w}}|_{E^{\mathrm{DG}}}\cdot\boldsymbol{n}_e + \delta_{\mathrm{FV}}K|_{E^{\mathrm{FV}}}\lambda_t(\psi(p_c|_{E^{\mathrm{FV}}}))\frac{p_{\mathrm{w}}|_{E^{\mathrm{FV}}} - p_{\mathrm{w}}|_{E^{\mathrm{DG}}}}{\tilde{h}}. \tag{29}$$

The parameter $\tilde{h}$ is the distance between the center of gravity of E^{FV} and the face e; therefore it takes piecewise constant values over the interface Γ^{DF}. The weights $\delta_{\mathrm{DG}}, \delta_{\mathrm{FV}}$ follow (14) with $\delta_{\mathrm{DG}} = \delta_e^-$ and $\delta_{\mathrm{FV}} = \delta_e^+$. Similarly, we have for the diffusive flux $K\lambda_{\mathrm{n}}\nabla p_{\mathrm{c}}\cdot\boldsymbol{n}_e$:

$$K\lambda_{\mathrm{n}}\nabla p_{\mathrm{c}}\cdot\boldsymbol{n}_e \approx \delta_{\mathrm{DG}}K|_{E^{\mathrm{DG}}}\lambda_{\mathrm{n}}(\psi(p_c|_{E^{\mathrm{DG}}}))\nabla p_c|_{E^{\mathrm{DG}}}\cdot\boldsymbol{n}_e + \delta_{\mathrm{FV}}K|_{E^{\mathrm{FV}}}\lambda_{\mathrm{n}}(\psi(p_c|_{E^{\mathrm{FV}}}))\frac{p_c|_{E^{\mathrm{FV}}} - p_c|_{E^{\mathrm{DG}}}}{\tilde{h}}. \tag{30}$$

Based on these approximations, we define the form γ_{DF} that couples the DG and FV solutions for (7).

$$\gamma_{\mathrm{DF}}(P_c, P_w, v) = -\sum_{e\in\Gamma^{\mathrm{DF}}}\int_e \delta_{\mathrm{DG}}\left(\lambda_t(\psi(P_c|_{E^{\mathrm{DG}}}))(K\nabla P_w)|_{E^{\mathrm{DG}}} + \lambda_{\mathrm{n}}(\psi(P_c|_{E^{\mathrm{DG}}}))(K\nabla P_c)|_{E^{\mathrm{DG}}}\right)\cdot \boldsymbol{n}_e[v]$$
$$+\sum_{e\in\Gamma^{\mathrm{DF}}}\int_e\left(\frac{\delta_{\mathrm{FV}}K|_{E^{\mathrm{FV}}}\lambda_t(\psi(P_c|_{E^{\mathrm{FV}}}))}{\tilde{h}}+\frac{\sigma_0}{h}\right)[P_w][v]+\sum_{e\in\Gamma^{\mathrm{DF}}}\int_e\left(\frac{\delta_{\mathrm{FV}}K|_{E^{\mathrm{FV}}}\lambda_{\mathrm{n}}(\psi(P_c|_{E^{\mathrm{FV}}}))}{\tilde{h}}\right)[P_c][v], \tag{31}$$

for any P_w, P_c, v in X_h. We define the penalty parameter σ_0 by the harmonic average of the product of permeability and total mobility:

$$\sigma_0 = 2\mathcal{H}\left(K|_{E^{\mathrm{DG}}}\lambda_t(\psi(P_c|_{E^{\mathrm{DG}}})), K|_{E^{\mathrm{FV}}}\lambda_t(\psi(P_c|_{E^{\mathrm{FV}}}))\right). \tag{32}$$

We remark that the traces of the unknowns on the DG element are linear polynomials on a given edge whereas the traces of the unknowns on the FV element are constants. Numerical quadrature is used to compute the integral on each edge in (31).

We now consider the interface fluxes arising from (8). The diffusive term $-\nabla\cdot(K\lambda_{\mathrm{n}}\nabla p_c)$ is handled as above. For the advective term, $\nabla\cdot((\lambda_{\mathrm{n}}/\lambda_t)\boldsymbol{u})$, we employ an upwind technique to evaluate the nonlinear term $\lambda_{\mathrm{n}}/\lambda_t$. We define the form η_{DF} that couples the FV and DG solutions for (8).

$$\eta_{\mathrm{DF}}(P_c, P_w, v) = -\sum_{e\in\Gamma^{\mathrm{DF}}}\int_e \delta_{\mathrm{DG}}\lambda_{\mathrm{n}}(\psi(P_c|_{E^{\mathrm{DG}}}))(K\nabla P_c)|_{E^{\mathrm{DG}}}\cdot\boldsymbol{n}_e[v]$$
$$+\sum_{e\in\Gamma^{\mathrm{DF}}}\int_e\left(\frac{\lambda_{\mathrm{n}}}{\lambda_t}\right)^{\uparrow}U_{\mathrm{DF}}[v]+\sum_{e\in\Gamma^{\mathrm{DF}}}\int_e\left(\frac{\delta_{\mathrm{FV}}K|_{E^{\mathrm{FV}}}\lambda_{\mathrm{n}}(\psi(P_c|_{E^{\mathrm{FV}}}))}{\tilde{h}}+\frac{\sigma_1}{h}\right)[P_c][v], \tag{33}$$

for any P_w, P_c, v in X_h. Using the same notation used above, $e=\partial E^{\mathrm{DG}}\cap\partial E^{\mathrm{FV}}$, we define the penalty parameter σ_1 by:

$$\sigma_1 = 2(\lambda_{\mathrm{n}}(\psi(P_c|_{E^{\mathrm{DG}}}))+\lambda_{\mathrm{n}}(\psi(P_c|_{E^{\mathrm{FV}}})))\,\mathcal{H}(K|_{E^{\mathrm{DG}}}, K|_{E^{\mathrm{FV}}}). \tag{34}$$

The discrete flux U_{DF} is defined on $e\in\Gamma_{\mathrm{DF}}$ by

$$U_{\mathrm{DF}} = -\delta_{\mathrm{DG}}\lambda_t(\psi(P_c|_{E^{\mathrm{DG}}}))(K\nabla P_w)|_{E^{\mathrm{DG}}}\cdot\boldsymbol{n}_e$$
$$-\left(\delta_{\mathrm{FV}}K|_{E^{\mathrm{FV}}}\frac{\lambda_t(\psi(P_c|_{E^{\mathrm{FV}}}))}{\tilde{h}}+\frac{\sigma_0}{h}\right)(P_w|_{E^{\mathrm{FV}}}-P_w|_{E^{\mathrm{DG}}}). \tag{35}$$

The upwind value on a face $e\in\Gamma_{\mathrm{DF}}$ is defined as follows:

$$\left(\frac{\lambda_{\mathrm{n}}}{\lambda_t}\right)^{\uparrow} = \begin{cases} \frac{\lambda_{\mathrm{n}}(\psi(P_c))}{\lambda_t(\psi(P_c))}\Big|_{E^{\mathrm{DG}}}, & \text{if} \quad U_{\mathrm{DF}}>0,\\ \frac{\lambda_{\mathrm{n}}(\psi(P_c))}{\lambda_t(\psi(P_c))}\Big|_{E^{\mathrm{FV}}}, & \text{if} \quad U_{\mathrm{DF}}\le 0.\end{cases} \tag{36}$$

3.5. Fully discrete scheme

We employ a first order backward Euler time stepping method. The time interval $(0, T)$ is partitioned into uniform intervals with length equal to the time step $\Delta t>0$. Let t^ℓ denote the time $\ell\Delta t$. The fully discrete scheme is: find $(P_{\mathrm{w}}^{\ell+1}, P_c^{\ell+1})\in X_h\times X_h$ for $\ell\ge 0$ satisfying:

$$a_{\mathrm{D}}(P_c^{\ell+1}, P_{\mathrm{w}}^{\ell+1}, v)+a_{\mathrm{F}}(P_c^{\ell+1}, P_{\mathrm{w}}^{\ell+1}, v)+\gamma_{\mathrm{DF}}(P_c^{\ell+1}, P_{\mathrm{w}}^{\ell+1}, v) = L_1(v), \tag{37}$$
$$-\int_\Omega\phi\frac{\psi(P_c^{\ell+1})-\psi(P_c^{\ell})}{\Delta t}v+b_{\mathrm{D}}(P_c^{\ell+1}, P_{\mathrm{w}}^{\ell+1}, v)+b_{\mathrm{F}}(P_c^{\ell+1}, P_{\mathrm{w}}^{\ell+1}, v)+\eta_{\mathrm{DF}}(P_c^{\ell+1}, P_{\mathrm{w}}^{\ell+1}, v) = L_2(v), \tag{38}$$

for all v in X_h. The initial value P_c^0 is the L^2 projection of p_c^0 in X_h. The right-hand side forms L_1 and L_2 are defined below. They contain the boundary data.

$$L_1(v) = -\int_{\Gamma_{\mathrm{N}}^{\mathrm{DG}}\cup\Gamma_{\mathrm{N}}^{\mathrm{FV}}}(j_w+j_n)v+\int_{\Gamma_{\mathrm{D}}^{\mathrm{DG}}}\frac{2K}{h}\lambda_t(\psi(g_{\mathrm{n}}-g_{\mathrm{w}}))\,g_{\mathrm{w}}v. \tag{39}$$

$$L_2(v) = -\int_{\Gamma_{\mathrm{N}}^{\mathrm{DG}}\cup\Gamma_{\mathrm{N}}^{\mathrm{FV}}}j_n v+\int_{\Gamma_{\mathrm{D}}^{\mathrm{DG}}}\frac{K}{h}\lambda_{\mathrm{n}}(\psi(g_{\mathrm{n}}-g_{\mathrm{w}}))\,(g_{\mathrm{n}}-g_{\mathrm{w}})v. \tag{40}$$

Table 1
Physical parameters used in the convergence rate study.

Parameter	Value
μ_{w}	10^{-3} Pa s
μ_{n}	9×10^{-4} Pa s
K	3.72×10^{-13} m^2
ϕ	0.2
$k_{r\mathrm{n}}$	$(1 - s_{\mathrm{w}})^2$
$k_{r\mathrm{w}}$	s_{w}^2
p_e	755 Pa
θ	2.5

Table 2
DGFV convergence rates for sinusoidal exact solution.

h	$\|\|p_{\mathrm{w}} - P_{\mathrm{w}}\|\|_{L^2(\Omega)}$	Conv. rate (p_{w})	$\|\|p_c - P_c\|\|_{L^2(\Omega)}$	Conv. rate (p_c)
1/10	1.19×10^{-1}	–	1.01×10^{-1}	–
1/20	5.27×10^{-2}	1.18	4.89×10^{-2}	1.05
1/40	2.59×10^{-2}	1.02	2.42×10^{-2}	1.01
1/80	1.30×10^{-2}	0.99	1.21×10^{-2}	1.00
1/160	6.48×10^{-3}	1.00	6.04×10^{-3}	1.00

Remark. We note that neither slope limiter nor H(div) projection of velocity is used. We observe throughout our simulations, the overshoot and undershoot associated with the DG method remain bounded and stable.

Remark. Scalar absolute permeability is used in place of matrix-valued permeability for simplicity. It is straightforward to employ matrix-valued permeabilities in regions that are interior to the DG subdomains, as it was done for diffusion problems in [4]. However, we do not recommend allowing for matrix-valued permeability in the FV subdomains, because this requires careful construction of grids and this defeats the purpose of using the DG-FV approach.

4. Numerical results

The multinumeric scheme has been implemented in the DUNE framework [27–30]. The nonlinear system is solved by inexact Newton where the Jacobian is approximated by a finite difference. The linear solver is BiCGStab with AMG preconditioner and SSOR smoother. For all the numerical tests, the domain is $\Omega = [0, 1] \times [0, 0.6]$ and it is partitioned into a structured mesh of square elements. We recall we solve for the discrete wetting phase pressure and capillary pressure at each time step. We will show in this section snapshots of the non-wetting phase saturation, which are obtained from (2) and from the discrete capillary pressure (see (5)).

4.1. Convergence rate study

We verify the accuracy of the proposed method for smooth solutions by computing convergence rates. The interface Γ^{DF} is the vertical segment $\{0.5\} \times [0, 0.6]$ and the subdomains are $\Omega^{\mathrm{DG}} = (0, 0.5) \times (0, 0.6)$ and $\Omega^{\mathrm{FV}} = (0.5, 1) \times (0, 0.6)$. Physical parameters are given in Table 1, and Dirichlet boundary conditions are assigned along all boundaries. Functions are evaluated and integration is performed using Gauss quadrature points.

The first set of exact solutions considered is:

$$p_{\mathrm{w}}(x, y) = 2 + \sin(2\pi x) \sin\left(\frac{2\pi}{0.6} y\right), \quad p_c(x, y) = 2 + \cos(2\pi x) \cos\left(\frac{2\pi}{0.6} y\right).$$

Table 2 displays the numerical errors and convergence rates. The coarsest mesh is of size $h = 0.1$, and each successive refinement divides each element into four elements. We observe the method converges with order one.

Table 3
DGFV convergence rates for the time-dependent sinusoidal exact solution.

h	Δt	$\|\|p_w - P_w\|\|_{L^2(\Omega)}$	Conv. rate (p_w)	$\|\|p_c - P_c\|\|_{L^2(\Omega)}$	Conv. rate (p_c)
1/10	1	1.13×10^{-1}	–	1.02×10^{-1}	–
1/20	1/2	5.21×10^{-2}	1.12	4.91×10^{-2}	1.05
1/40	1/4	2.55×10^{-2}	1.03	2.42×10^{-2}	1.02
1/80	1/8	1.27×10^{-2}	1.01	1.21×10^{-2}	1.00
1/160	1/16	6.37×10^{-3}	1.00	6.04×10^{-3}	1.00

The second set of exact solutions considered is:

$$p_w(t, x, y) = 2 + \sin(2\pi x)\sin\left(\frac{2\pi}{0.6}y\right) + t, \quad p_c(t, x, y) = 2 + \cos(2\pi x)\cos\left(\frac{2\pi}{0.6}y\right) + \frac{t^2}{2}.$$

Table 3 displays the numerical errors and convergence rates. As before, the coarsest mesh is of size $h = 0.1$, and each successive refinement divides each element into four elements. As the mesh is successively refined, the time-step Δt is also decreased by a factor of 2 each time, with the final time T being set at $T = 1$ s. We again observe the method converges with order one.

4.2. Homogeneous medium

We consider two choices for the multinumeric method. First, the domain Ω is split into two subdomains: $\Omega^{DG} = [0, 0.5] \times [0, 0.6]$ and $\Omega^{FV} = [0.5, 1] \times [0, 0.6]$. This means that we use the discontinuous Galerkin method on the left-half of the domain and the finite volume method on the right. This is denoted as the "DGFV" method. Second, we set $\Omega^{FV} = [0, 0.5] \times [0, 0.6]$ and $\Omega^{DG} = [0.5, 1] \times [0, 0.6]$. Here, we use the FV method on the left-half of the domain and the DG method on the right; this is denoted as the "FVDG" method. In both cases, $\Gamma^{DF} = \{0.5\} \times [0, 1]$.

The Neumann boundary is the union of $[0, 1] \times \{0\}$ and $[0, 1] \times \{0.6\}$. The Neumann boundary data is set to zero: $j_w = j_n = 0$. The Dirichlet datum (see (9)) is:

$$g_w = 2 \times 10^4 \text{ Pa}, \quad g_n - g_w = 1.896 \times 10^3 \text{ Pa}, \quad \text{on} \quad \{0\} \times [0, 0.6], \tag{41}$$

$$g_w = 0 \text{ Pa}, \quad g_n - g_w = 7.87 \times 10^2 \text{ Pa}, \quad \text{on} \quad \{1\} \times [0, 0.6]. \tag{42}$$

The Dirichlet boundary conditions on p_c means that the non-wetting phase saturation is prescribed equal to 0.9 on the left boundary $\{0\} \times [0, 0.6]$ and equal to 0.1 on the right boundary $\{1\} \times [0, 0.6]$. Table 1 shows the physical parameters used in this example. Finally for discretization parameters, the mesh consists of 40×24 squares of side $h = 0.025$. The final time is $T = 25\,000$ s and the time step is $\Delta t = 100$ s.

We compare the numerical solutions obtained from (37)–(38) with the solutions obtained by either using the finite volume method everywhere in Ω (referred to as "all FV" method) or the discontinuous Galerkin method everywhere (referred to as "all DG" method). The non-wetting saturation profiles along the line $y = 0.3$ are shown in Fig. 2 for the three methods: all FV, all DG and DGFV. We observe as expected that before the front reaches the interface, the DG and DGFV saturation fronts are sharper than the FV saturation front. The DG solution exhibits a small undershoot whereas the FV saturation is bounded from below by zero. Once the DGFV saturation front passes through the interface, the undershoot disappears. The proposed scheme does not use any slope limiting or any H(div) projection of the velocity. We also note that the location of the front for the DGFV solution coincides with the location of the front for the DG solution whereas the location of the front for the FV solution is slightly behind.

Similarly, Fig. 3 shows the saturation profiles for FVDG, all FV and all DG. We observe that the FV and FVDG saturation fronts coincide before the front reaches the interface. Once the front is located in the DG region, a small undershoot appears at the front and disappears at later times.

The results for the homogeneous medium show the accuracy of the proposed coupled FV and DG scheme. Computational times are displayed in Table 4 for the DGFV scheme and the DG scheme ran on a single processor with different mesh sizes. The code was run on an Intel Xeon E5-2650 v2 2.60 GHz processor. Table 4 shows that the DGFV multinumeric method is between 29% and 46% faster than the DG method.

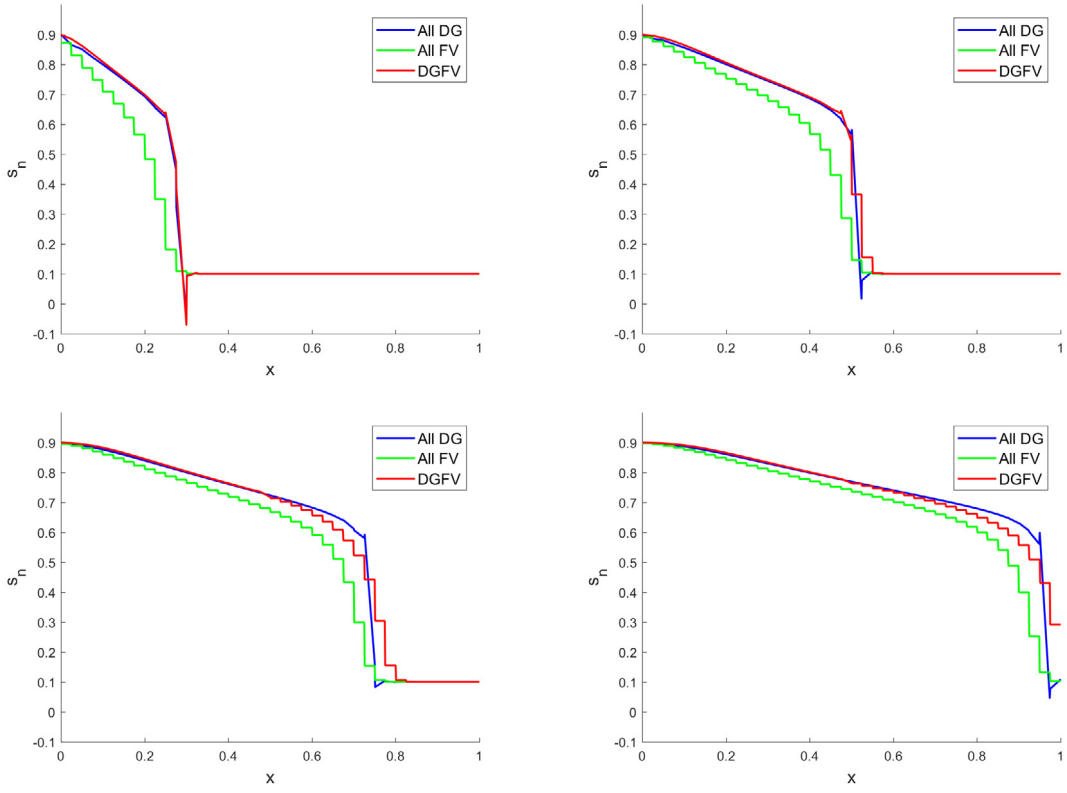

Fig. 2. Saturation curves for three methods: DGFV, DG, FV at times 5500 s, 11 000 s, 16 500 s, and 22 000 s.

Table 4
Timing results for the DGFV method compared to the DG and FV methods, for different levels of mesh refinement.

Mesh spacing	Method	Unknowns	Simulation time
0.1	All FV	60	0.75 s
	DGFV	150	5.06 s
	All DG	240	9.39 s
0.05	All FV	240	4.12 s
	DGFV	600	28.13 s
	All DG	960	39.50 s
0.025	All FV	960	7.39 s
	DGFV	2400	103.13 s
	All DG	3840	155.50 s

4.3. Porous medium with low permeability block

The permeability field takes the value K_1 in most of the domain and the value K_2 in a rectangular inclusion of width 0.1 and height 0.3. The inclusion is placed symmetrically around three different points: $(0.25, 0.3)$, $(0.45, 0.3)$ and $(0.5, 0.3)$. These three set-ups are referred to as case A, case B and case C. Fig. 4 displays the set-up for the interface Γ_{DF} (which is the vertical segment $\{0.5\} \times [0, 0.6]$) and the permeability inclusion. The permeability in the inclusion is $K_2 = 10^{-3} K_1$, with $K_1 = 3.72 \times 10^{-13}$ m^2.

We choose $\theta = 2$ for (4). The remaining physical parameters are the same as in the previous section. Figs. 5 and 6 show the saturation contours for the non-wetting phase at different times, $t = 6200$, 12 500, 18 700 and 25 000 s,

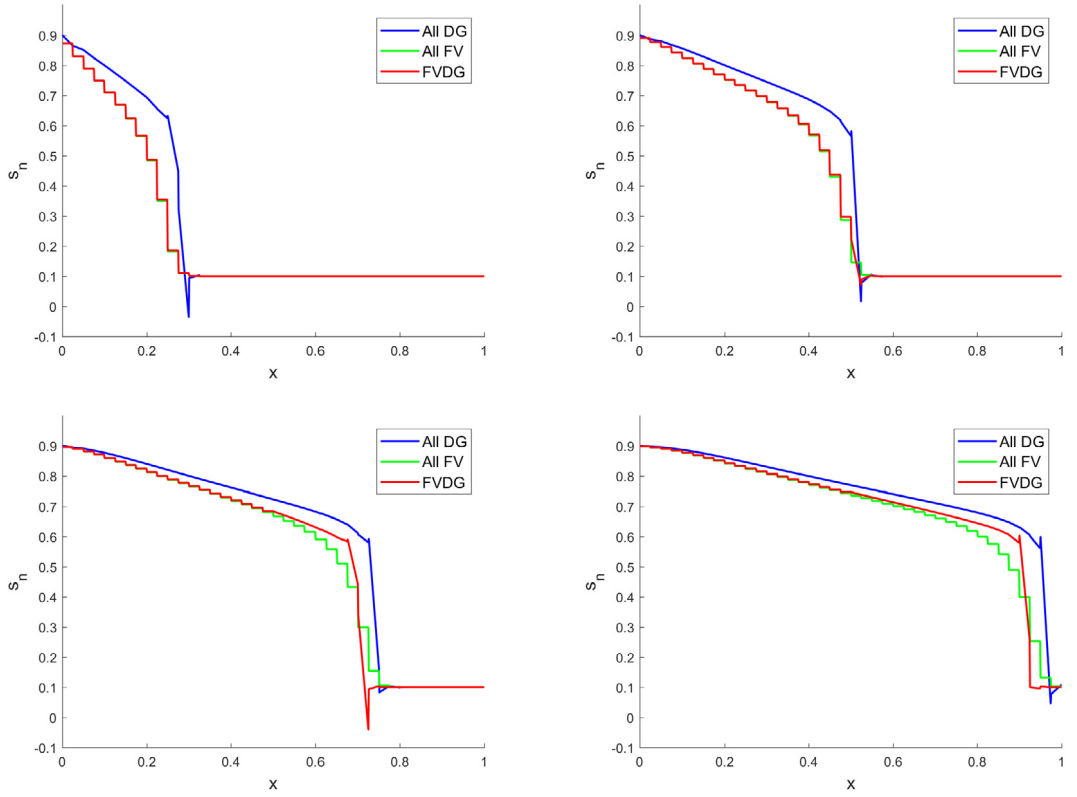

Fig. 3. Saturation curves for the FVDG, DG, FV methods at times 5500 s, 11 000 s, 16 500 s, and 22 000 s.

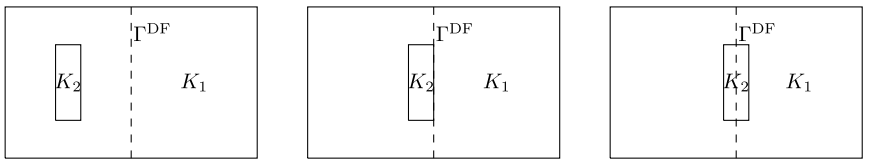

Fig. 4. Porous medium with lower permeability block ($K_2 = 10^{-3}K_1$) at three different positions with respect to interface: case A (left), case B (center) and case C (right).

for case A where the lower permeability region is entirely in the left region. As in the previous section, we refer to the DGFV method the coupled method for which the left region is Ω^{DG} and the right region is Ω^{FV}. If we switch the allocation of the methods to the domains, we obtain the FVDG method. Fig. 5 shows time snapshots for the DGFV method whereas Fig. 6 displays snapshots for the FVDG method.

Figs. 7 and 8 show the saturation contours for Case B obtained with DGFV and FVDG respectively. Figs. 9 and 10 show the saturation contours for Case C obtained with DGFV and FVDG respectively. The location of the saturation front naturally depends on the location of the lower permeability block. The three different cases show the robustness of the multinumeric scheme with respect to the location of the interface in the domain with non-homogeneous permeability.

4.4. Heterogeneous porous medium

In this example, the permeability field is varying in space following [31]. In Fig. 11, the permeability in the gray squares is $K_1 = 3.72 \times 10^{-13}$ m^2 and the permeability in the black squares is $K_2 = 10^{-4}K_1$. We choose $\theta = 2$

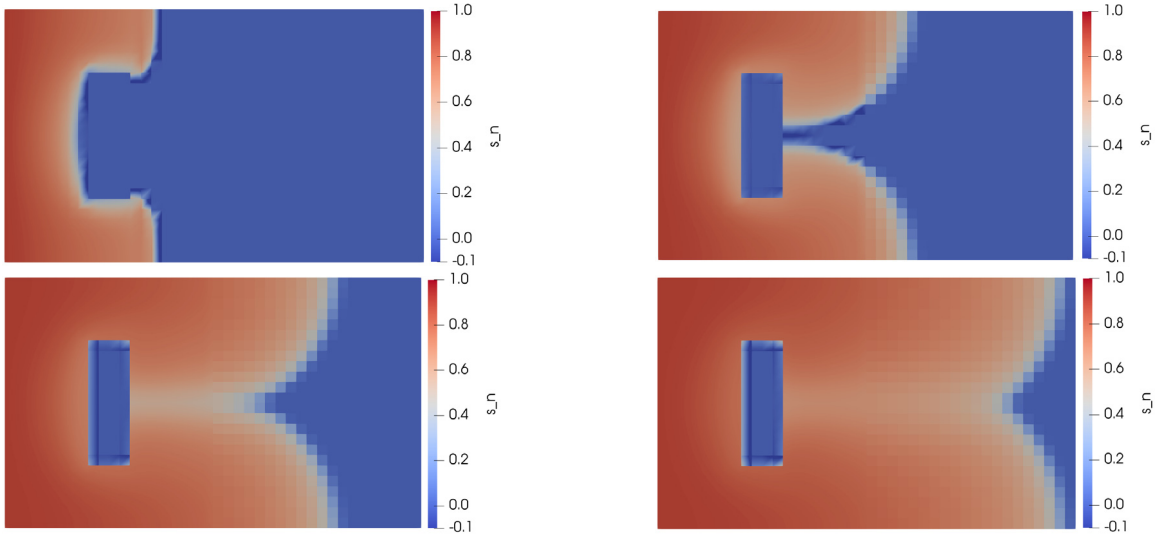

Fig. 5. Non-wetting phase saturation contours with DGFV method: Ω^{DG} is the left subdomain. Permeability inclusion corresponds to case A. Snapshots at $t = 6200, 12\,500, 18\,700$ and $25\,000$ s.

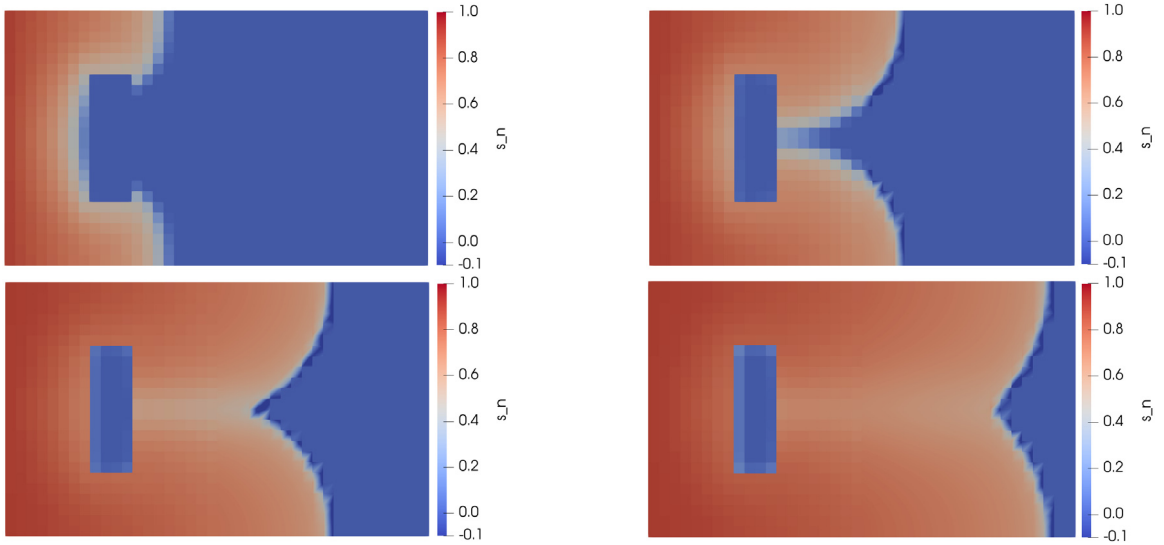

Fig. 6. Non-wetting phase saturation contours with FVDG method: Ω^{FV} is the left subdomain. Permeability inclusion corresponds to case A. Snapshots at $t = 6200, 12\,500, 18\,700$ and $25\,000$ s.

for (4). The other physical parameters are the same as in Table 1. Boundary conditions and spatial discretization parameters are the same as in Section 4.2.

First we partition the domain such that the interface is the vertical segment $\{0.5\} \times [0, 0.6]$. Fig. 12 shows the saturation snapshots at times $t = 7500, 15\,000, 22\,500$ and $30\,000$ s. The method DGFV is employed. We observe the saturation avoids the small regions where the permeability is much smaller than in the rest of the domain. Snapshots of the pressure are shown in Fig. 13).

Similarly, Fig. 14 (resp. Fig. 15) shows the contours of the saturation (resp. pressure) at the same times for the FVDG method. As expected, the saturation fronts are more diffusive if they are located in the FV region.

We now change the partition of the domain and select for Ω^{DG} an inner square that encloses the regions with smaller permeability (see the location of the interface Γ_{DF} in Fig. 16).

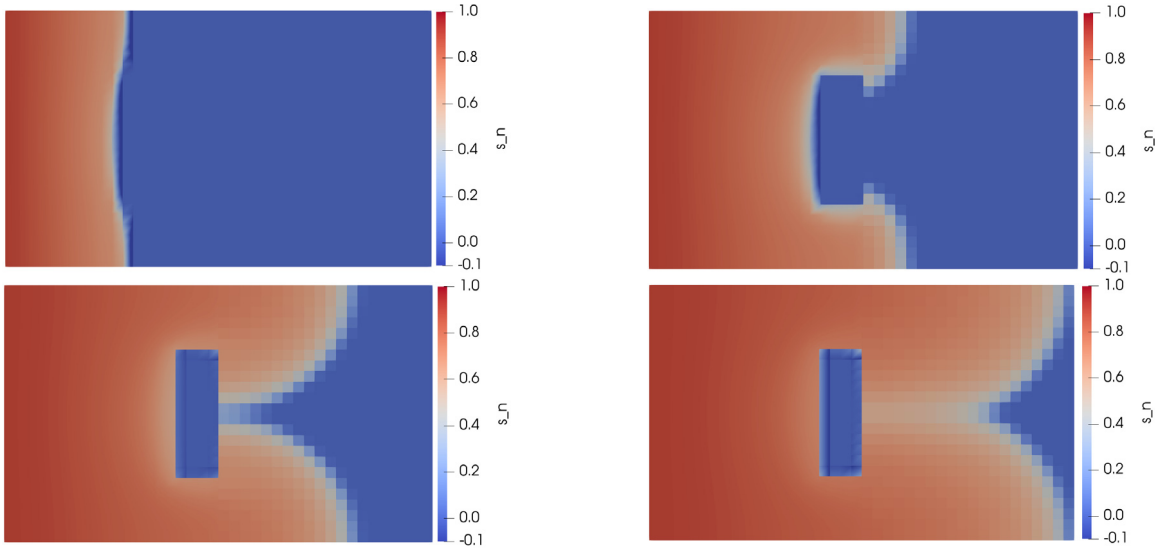

Fig. 7. Non-wetting phase saturation contours with DGFV method: Ω^{DG} is the left subdomain. Permeability inclusion corresponds to case B. Snapshots at $t = 6200, 12\,500, 18\,700$ and $25\,000$ s.

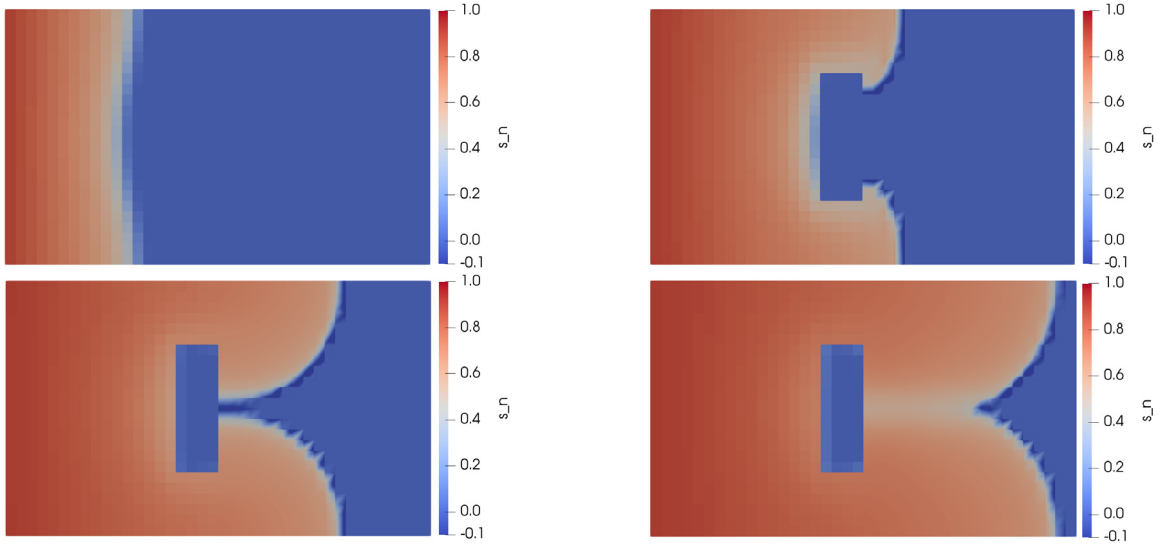

Fig. 8. Non-wetting phase saturation contours with FVDG method: Ω^{FV} is the left subdomain. Permeability inclusion corresponds to case B. Snapshots at $t = 6200, 12\,500, 18\,700$ and $25\,000$ s.

The non-wetting phase saturation contours are shown at times 7500 s, 15 000 s, 22 500 s, and 30 000 s in Fig. 17. The pressure contours are given in Fig. 18. Results are consistent with the ones obtained above. However there are some differences in the location of the front at time $t = 30\,000$ s. Table 5 gives the computational times for the multinumeric solution and for the DG solution. There is a significant gain in using the multinumeric solution: it is 68% faster than the DG solution.

4.5. Heterogeneous medium with channels

In this example, the domain contains three channels in which the permeability is significantly higher than in the surrounding rock. The permeability in the rock matrix varies in space between 10^{-13} m^2 and 5×10^{-13} m^2

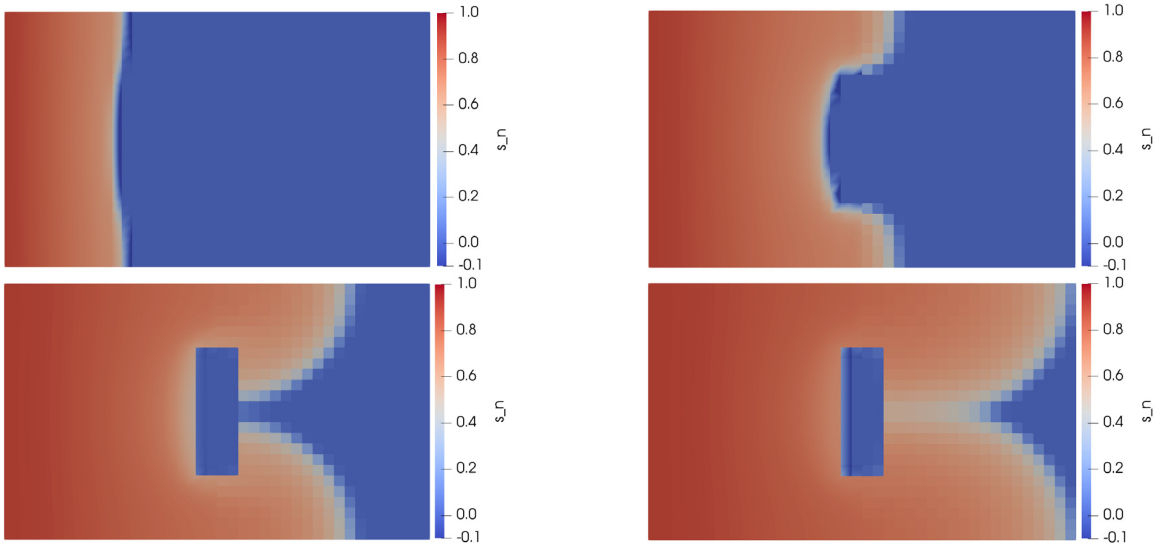

Fig. 9. Non-wetting phase saturation contours with DGFV method: Ω^{DG} is the left subdomain. Permeability inclusion corresponds to case C. Snapshots at $t = 6200, 12\,500, 18\,700$ and $25\,000$ s.

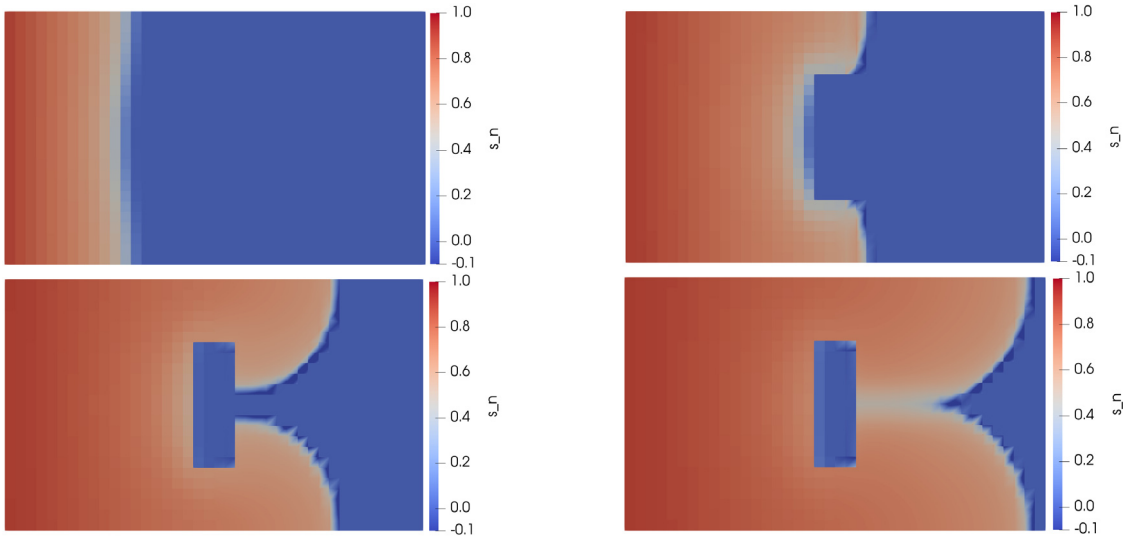

Fig. 10. Non-wetting phase saturation contours with FVDG method: Ω^{FV} is the left subdomain. Permeability inclusion corresponds to case C. Snapshots at $t = 6200, 12\,500, 18\,700$ and $25\,000$ s.

Table 5
Timing results for the multinumeric method compared to the DG and FV methods.

Method	Unknowns	Time to solution
All FV	960	130.96 s
Multinumeric	2160	1650.56 s
DG	3840	5154.73 s

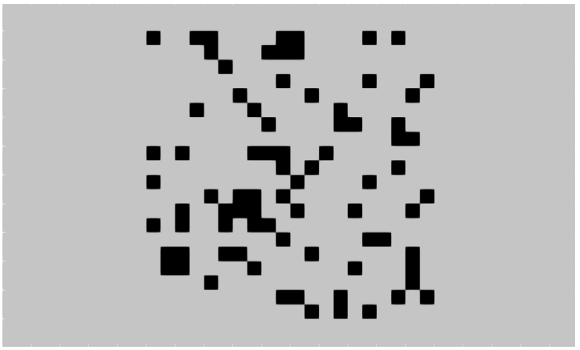

Fig. 11. Permeability field: gray squares have a permeability K_1 =3.72e−13 m^2 and black squares have a permeability $K_2 = 10^{-4}K_1$.

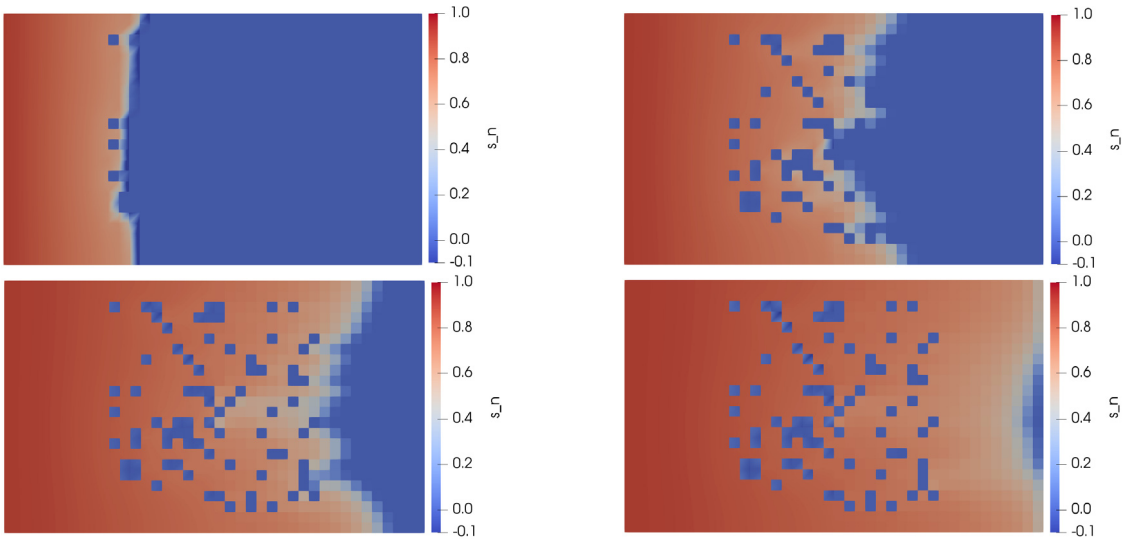

Fig. 12. Non-wetting phase saturation snapshots for DGFV for heterogeneous medium at times 7500 s, 15 000 s, 22 500 s, and 30 000 s.

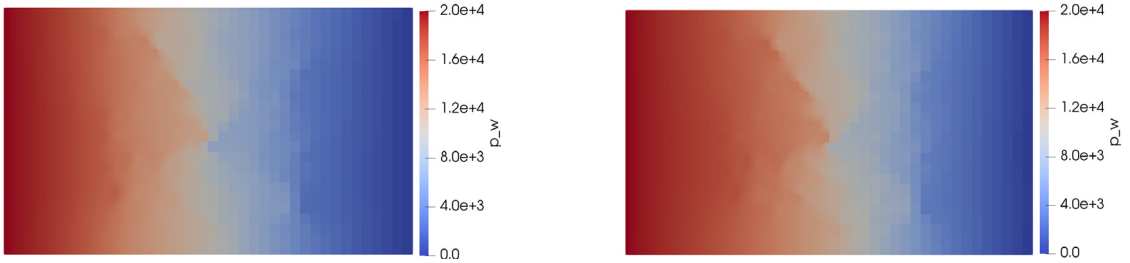

Fig. 13. Wetting phase pressure snapshots for DGFV for heterogeneous medium at times 7500 s and 30 000 s.

whereas the permeability in the channels is equal to 10^{-10} m^2. Further, we partition the domain such that the DG method is used in a neighborhood including each channel and the FV method is used elsewhere. Fig. 19 shows the permeability field in the rock matrix, the location of the channels and the partition of the domain into Ω^{FV} and Ω^{DG}. The physical parameters are the same as in Table 1. Boundary conditions and spatial discretization parameters are the same as in Section 4.2.

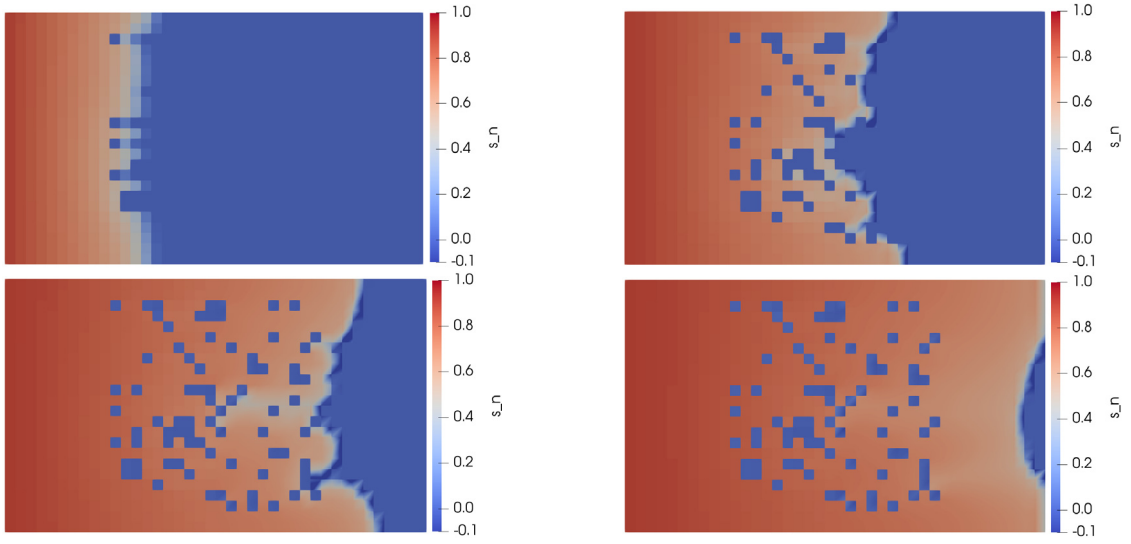

Fig. 14. Non-wetting phase saturation snapshots for FVDG for heterogeneous medium at times 7500 s, 15 000 s, 22 500 s, and 30 000 s.

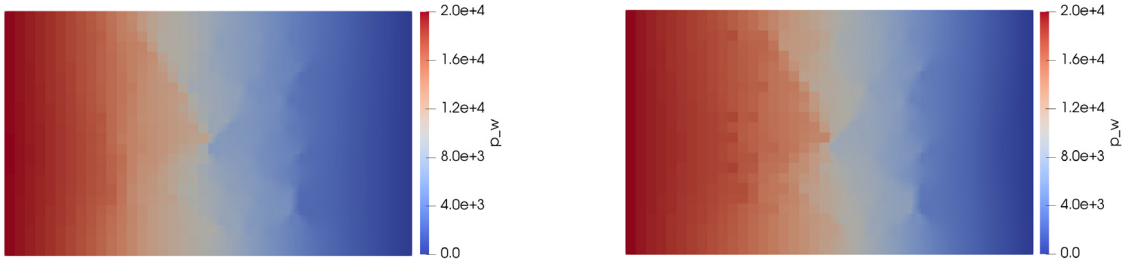

Fig. 15. Wetting phase pressure snapshots for FVDG for heterogeneous medium at times 7500 s and 30 000 s.

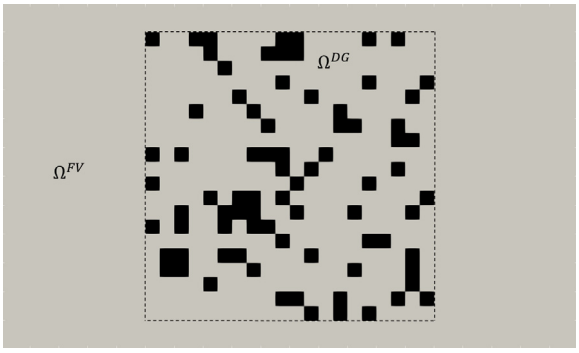

Fig. 16. Permeability field: gray squares have a permeability K_1 =3.72e−13 m^2 and black squares have a permeability $K_2 = 10^{-4}K_1$.

Figs. 20 and 21 show the saturation and pressure snapshots at times $t = 4000, 6000, 13\,000$, and $20\,000$ s, respectively. As expected, the injected phase floods the channel closest to the inflow boundary. As time advances, the saturation fronts are further advanced in the regions of the rock matrix where the permeability is larger. We also observe that the changes in the wetting phase pressure contours occur at a slower time scale. We compare the computational times for the multinumeric scheme with the DG scheme in Table 6. Results show that the multinumeric method is 86% faster than the DG method.

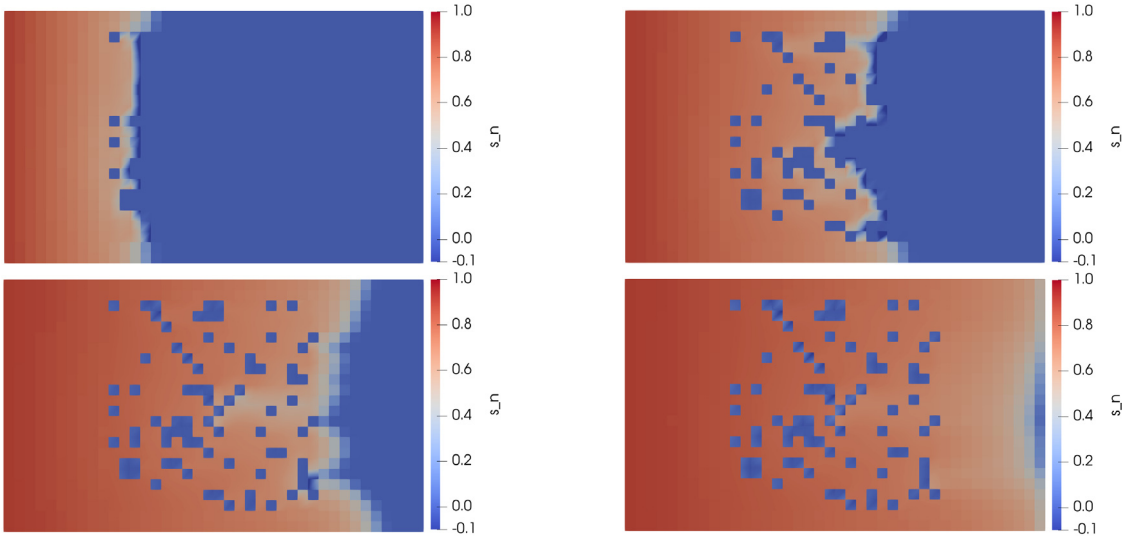

Fig. 17. Non-wetting phase saturation snapshots for heterogeneous medium when using DG for inner region at times 7500 s, 15 000 s, 22 500 s, and 30 000 s.

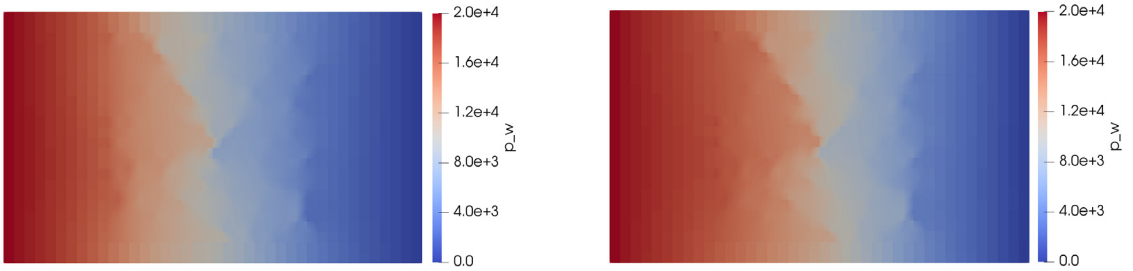

Fig. 18. Wetting phase pressure snapshots for heterogeneous medium when using DG for inner region at times 7500 s and 30 000 s.

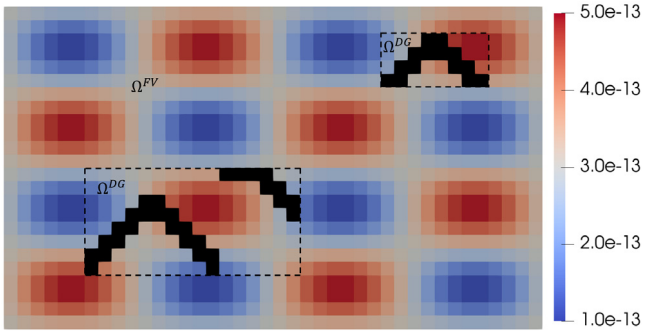

Fig. 19. Permeability field and domain partition. Channels are the black regions. (For interpretation of the references to color in this figure legend, the reader is referred to the web version of this article.)

In the final test, we repeat the simulation with one change of parameter. We now select a smaller value for $\theta = 1$. Fig. 22 shows the contours for the non-wetting phase saturation and wetting phase pressure at time $t = 6000$ s. We observe a more diffuse saturation front in this case, compared to the case $\theta = 2.5$ (Fig. 20).

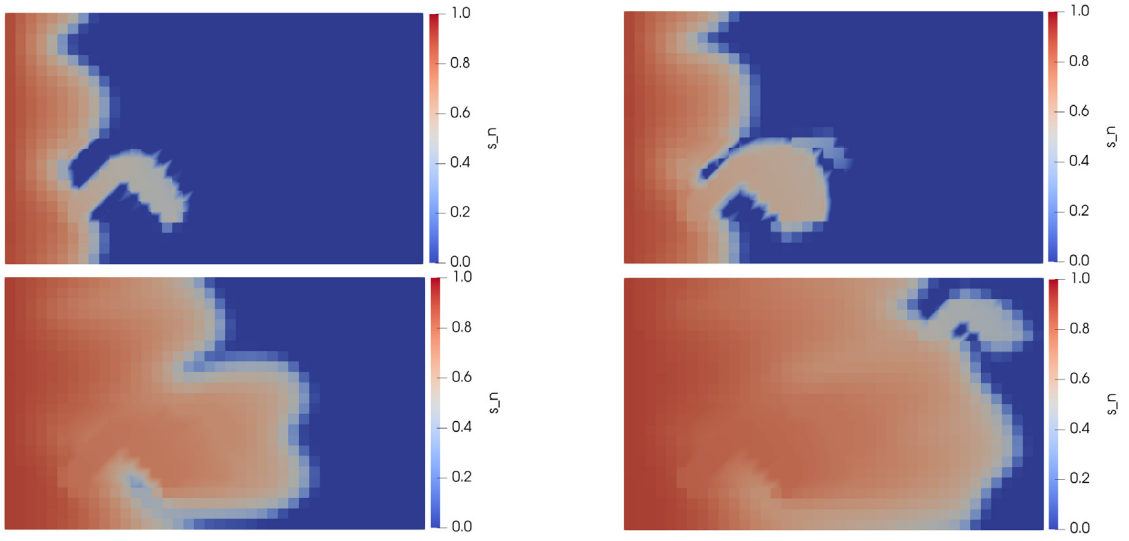

Fig. 20. Non-wetting phase saturation snapshots for channel scenario at times 4000 s, 6000 s, 13 000 s, and 20 000 s.

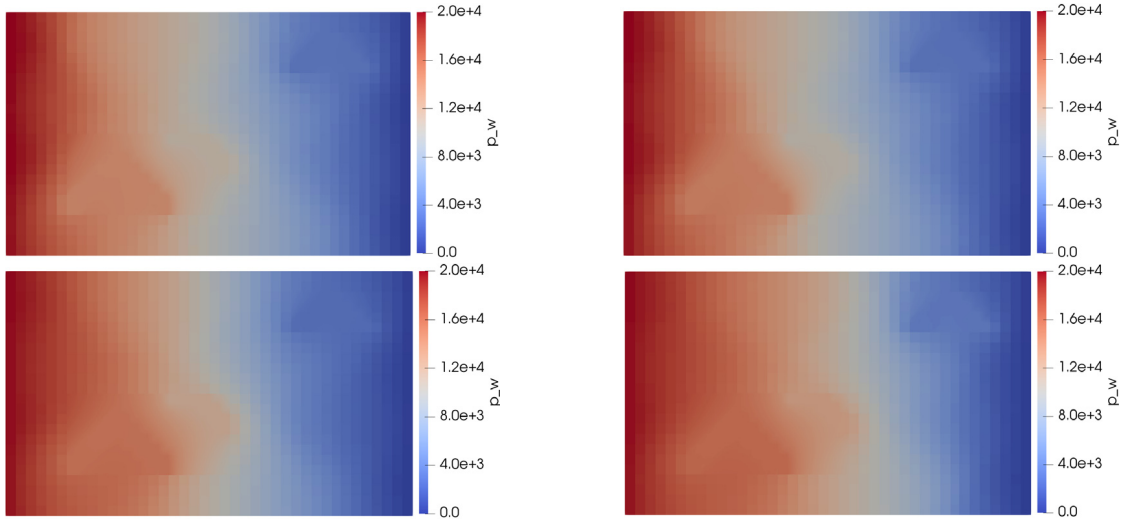

Fig. 21. Wetting phase pressure snapshots for channel scenario at times 4000 s, 6000 s, 13 000 s, and 20 000 s.

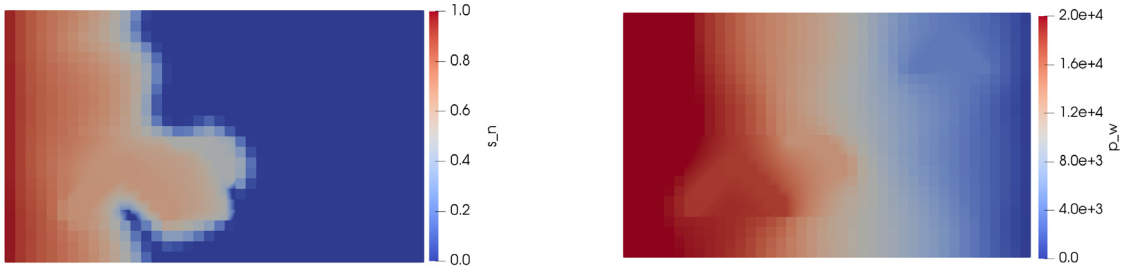

Fig. 22. Non-wetting phase saturation and wetting phase pressure snapshots for channel scenario at time 6000 s, when the parameter $\theta = 1$.

Table 6
Timing results for the multinumeric method compared to the DG method, for the channel flow scenario.

Method	Unknowns	Time to solution
Multinumeric	1440	732.99 s
DG	3840	5160.94 s

5. Conclusions

This paper formulates a method that combines the interior penalty discontinuous Galerkin method with the cell-centered finite volume method for the incompressible two-phase flow problem. Meshes for the finite volume subdomains consist of rectangles or boxes whereas meshes for the discontinuous Galerkin subdomains are allowed to be structured or unstructured. The interface between the subdomains is treated implicitly by carefully designing the numerical fluxes between the two types of discretizations. The resulting fully implicit scheme solves for the wetting phase pressure and the capillary pressure. Numerical results for homogeneous and heterogeneous media show the robustness and efficiency of the multinumeric method. In our paper, the DG subdomains are selected such that they contain regions where the permeability is highly heterogeneous. In practice, DG regions should be regions where higher accuracy is needed and where FV solutions are too numerically diffusive. For instance, if there is a strong anisotropy in certain regions, or if there are local features such as pinch-outs or channels. In this case knowledge on the geological structure of the domain is the criterion to use for the allocation of DG and FV elements. In addition, it would be of interest to dynamically partition the domain so that the saturations fronts are located in DG elements. Away from the fronts, the FV elements would be used. In that case, the selection criterion is based on the magnitude of the gradient of the saturation.

Declaration of competing interest

The authors declare that they have no known competing financial interests or personal relationships that could have appeared to influence the work reported in this paper.

References

[1] D.W. Peaceman, Fundamentals of Numerical Reservoir Simulation, Vol. 6, Elsevier, 2000.
[2] K. Aziz, A. Settari, Petroleum Reservoir Simulation, Applied Science Publ. Ltd., London, UK, 1979.
[3] Z. Chen, G. Huan, Y. Ma, Computational Methods for Multiphase Flows in Porous Media, Vol. 2, SIAM, 2006.
[4] P. Chidyagwai, I. Mishev, B. Riviere, On the coupling of finite volume and discontinuous Galerkin method for elliptic problems, J. Comput. Appl. Math. 231 (2011) 2193–2204.
[5] B. Riviere, P. Chidyagwai, I. Mishev, On the coupling of finite volume and discontinuous Galerkin for reservoir simulation problems, in: SPE Reservoir Symposium, Society for Petroleum Engineers, 2011, No. SPE-141971-MS.
[6] B. Riviere, X. Yang, Convergence analysis of a coupled method for time-dependent convection–diffusion equations, Numer. Methods Partial Differential Equations 30 (1) (2014) 133–157.
[7] P. Forsyth, A control volume finite element approach to NAPL groundwater contamination, SIAM J. Sci. Stat. Comput. 12 (1991) 1029–1057.
[8] A. Michel, A finite volume scheme for the simulation of two-phase incompressible flow in porous media, SIAM J. Numer. Anal. 41 (2003) 1301–1317.
[9] B. Li, Z. Chen, G. Huan, Control volume function approximation methods and their applications to modeling porous media flow I: the two-phase flow, Adv. Water Resour. 26 (2003) 435–444.
[10] J. Droniou, Finite volume schemes for diffusion equations: introduction to and review of modern methods, Math. Models Methods Appl. Sci. 24 (08) (2014) 1575–1619.
[11] Martin Schneider, Dennis Gläser, Bernd Flemisch, Rainer Helmig, Comparison of finite-volume schemes for diffusion problems, Oil Gas Sci. Technol. Rev. IFP Energies Nouv. 73 (2018) 82.
[12] W. Klieber, B. Riviere, Adaptive simulations of two-phase flow by discontinuous Galerkin methods, Comput. Methods Appl. Mech. Engrg. 196 (2006) 404–419.
[13] Y. Epshteyn, B. Riviere, Fully implicit discontinuous finite element methods for two-phase flow, Appl. Numer. Math. 57 (2007) 383–401.
[14] A. Ern, I. Mozolevski, L. Schuh, Discontinuous Galerkin approximation of two-phase flows in heterogeneous porous media with discontinuous capillary pressures, Comput. Methods Appl. Mech. Engrg. 199 (23–24) (2010) 1491–1501.

[15] T. Arbogast, M. Juntunen, J. Pool, M.F. Wheeler, A discontinuous Galerkin method for two-phase flow in a porous medium enforcing H(div) velocity and continuous capillary pressure, Comput. Geosci. 17 (6) (2013) 1055–1078.
[16] P. Bastian, A fully-coupled discontinuous Galerkin method for two-phase flow in porous media with discontinuous capillary pressure, Comput. Geosci. 18 (5) (2014) 779–796.
[17] A. Taneja, J. Higdon, A fully-coupled discontinuous Galerkin spectral element method for two-phase flow in petroleum reservoirs, J. Comput. Phys. 352 (2018) 341–372.
[18] R. Helmig, Multiphase Flow and Transport Processes in the Subsurface: A Contribution to the Modeling of Hydrosystems, Springer-Verlag, 1997.
[19] M. Peszynska, Q. Lu, M.F. Wheeler, Coupling different numerical algorithms for two phase fluid flow, in: Proceedings of the Mathematics of Finite Elements and Applications, 1999, pp. 205–214.
[20] R. Huber, R. Helmig, Multiphase flow in heterogeneous porous media: A classical finite element method versus an implicit pressure–explicit saturation-based mixed finite element–finite volume approach, Internat. J. Numer. Methods Fluids 29 (8) (1999) 899–920.
[21] H. Hoteit, A. Firoozabadi, Numerical modeling of two-phase flow in heterogeneous permeable media with different capillarity pressures, Adv. Water Resour. 31 (1) (2008) 56–73.
[22] R. Brooks, T. Corey, Hydraulic properties of porous media, in: Hydrology Papers, vol. 24, Colorado State University, 1964, p. 37.
[23] M. Van Genuchten, A closed-form equation for predicting the hydraulic conductivity of unsaturated soils, Soil Sci. Soc. Am. 44 (1980) 892–898.
[24] A. Ern, A. Stephansen, P. Zunino, A discontinuous Galerkin method with weighted averages for advection–diffusion equations with locally small and anisotropic diffusivity, IMA J. Numer. Anal. 29 (2) (2008) 235–256.
[25] T.G.R. Eymard, R. Herbin, Finite volume methods, Tech. Sci. Comput. 7 (2000) 713–1020.
[26] B. Riviere, Discontinuous Galerkin Methods for Solving Elliptic and Parabolic Equations: Theory and Implementation, SIAM, 2008.
[27] M. Blatt, P. Bastian, On the generic parallelisation of iterative solvers for the finite element method, Int. J. Comput. Sci. Eng. 4 (1) (2008) 56–69.
[28] M. Blatt, A. Burchardt, A. Dedner, C. Engwer, J. Fahlke, B. Flemisch, C. Gersbacher, C. Gräser, F. Gruber, C. Grüninger, et al., The distributed and unified numerics environment, version 2.4, Arch. Numer. Softw. 4 (100) (2016) 13–29.
[29] P. Bastian, M. Blatt, A. Dedner, C. Engwer, R. Klöfkorn, M. Ohlberger, O. Sander, A generic grid interface for parallel and adaptive scientific computing. Part I: abstract framework, Computing 82 (2–3) (2008) 103–119.
[30] P. Bastian, M. Blatt, A. Dedner, C. Engwer, R. Klöfkorn, R. Kornhuber, M. Ohlberger, O. Sander, A generic grid interface for parallel and adaptive scientific computing. Part II: implementation and tests in DUNE, Computing 82 (2–3) (2008) 121–138.
[31] P. Bastian, B. Riviere, Superconvergence and H(div) projection for discontinuous Galerkin methods, Internat. J. Numer. Methods Fluids 42 (2003) 1043–1057.